Camera Auto-calibration from the Steiner Conic of the Fundamental Matrix

Yu LIU[1,2][0000−0003−3888−8095] and Hui ZHANG[2][0000−0002−1681−7926]

[1] Department of Computer Science, Hong Kong Baptist University
Hong Kong SAR, China,
[2] Guangdong Key Laboratory of Interdisciplinary Research and Application for Data Science, BNU-HKBU United International College, Zhuhai, China
{yuliu, amyzhang}@uic.edu.cn

Abstract. This paper addresses the problem of camera auto-calibration from the fundamental matrix under general motion. The fundamental matrix can be decomposed into a symmetric part (a Steiner conic) and a skew-symmetric part (a fixed point), which we find useful for fully calibrating camera parameters. We first obtain a fixed line from the image of the symmetric, skew-symmetric parts of the fundamental matrix and the image of the absolute conic. Then the properties of this fixed line are presented and proved, from which new constraints on general eigenvectors between the Steiner conic and the image of the absolute conic are derived. We thus propose a method to fully calibrate the camera. First, the three camera intrinsic parameters, i.e., the two focal lengths and the skew, can be solved from our new constraints on the imaged absolute conic obtained from at least three images. On this basis, we can initialize and then iteratively restore the optimal pair of projection centers of the Steiner conic, thereby obtaining the corresponding vanishing lines and images of circular points. Finally, all five camera parameters are fully calibrated using images of circular points obtained from at least three images. Experimental results on synthetic and real data demonstrate that our method achieves state-of-the-art performance in terms of accuracy.

Keywords: Auto-calibration, Steiner conic, Fundamental matrix, General motion

1 Introduction

Camera calibration is a very critical step in image measurement or machine vision applications such as 3D reconstruction [36], [23], [5], vision metrology [22] and robot navigation [4]. The accuracy and stability of the calibration algorithm directly affect its usability. In the past few decades, researchers have proposed many methods to solve the problem of camera calibration, which can be roughly divided into two categories: calibration with objects [37], [10], [35] and without objects [36], [7], [12], [34], [30]. Calibration methods with objects always require highly accurate tailor-made calibration objects, such as lines [37], 2D

planar patterns [36], [10], [15] or 3D objects [35], [32], [24], etc. These methods can accurately calibrate the camera parameters according to the geometric constraints provided by the calibration objects. However, the calibration process is manually cumbersome, which greatly limits the scope of application of these methods. In contrast, auto-calibration methods can recover the camera intrinsic parameters through corresponding points [7], [12], [31], [3], [21] or object contours in the scene images [34], [19], [30], [33], [26]. Since no specific objects are required, auto-calibration methods can avoid the tedious manual process, greatly expanding its application and can even be applied to pre-shot videos.

Researchers have successfully proposed closed-form solutions for auto-calibration under constrained motion, such as rotational motion [1], [2], planar motion [16], [6], [34], [29], etc. For pure rotation, the camera intrinsic parameters can be calibrated using the rotational conjugation of the infinite homography of the image pair [13]. For planar motion [16], [6], the translation is always perpendicular to the rotation axis. The vanishing point of the translation direction and the image of the rotation axis can be derived from the fundamental matrix, which provides a pole-polar relationship with respect to the image of the absolute conic for auto-calibration. In [34], [29], the authors calibrate the three intrinsic parameters using the imaged silhouettes of an object under turntable motion. However, due to insufficient geometric constraints, most of these existing methods can only calibrate a limited number of camera intrinsic parameters.

The first auto-calibration method for general motion used the Kruppa equation to obtain the camera intrinsic parameters [13], [7], [12], [31], [3], [21]. It uses the fundamental matrix as input to obtain the constraints on the dual image of the absolute conic, which is used for camera calibration. The Kruppa equation contains two independent constraints on the five unknown camera intrinsic parameters from two views under general motion. Therefore, at least three images can be used to fully calibrate the camera. Although algebraic solutions [13], [7], [28] are available, there are still 2^5 possible solutions for the five unknowns from the five quadratic equations [13]. Later in [21], a hybrid method of GA [17] & PSO [18] was proposed to optimize the accuracy of camera auto-calibration, which heavily depends on the initial values. Other approaches attempt to simplify the Kruppa equation by eliminating the scale coefficients by some specific operations, such as applying singular value decomposition (SVD) to the fundamental matrix [13], [7], [21], [11] or using the rank constraint on the coefficient matrix [20], [11]. However, there is still several ambiguity in the obtained constraints for camera auto-calibration. Therefore, the inaccuracy and ambiguity of these methods have made them lose their popularity.

This paper presents a two-step solution to the problem of camera auto-calibration using the fundamental matrix under general motion. The method is based on a newly discovered constraint derived from the Steiner conic, the symmetric part of the fundamental matrix. Inspired by the general eigenvectors of two separate conics [15], [14], we first obtain a fixed line from the image of the Steiner conic, the skew-symmetric part of the fundamental matrix and the image of the absolute conic. Then the properties of this fixed line are presented

and proved, from which new constraints on general eigenvectors between the Steiner conic and the image of the absolute conic are derived. We thus propose a method to fully calibrate the camera. First, the three parameters of the camera intrinsics, namely the two focal lengths and the skew, can be recovered by our new constraints on the imaged absolute conic from at least three images. On this basis, we can initialize and iteratively restore the optimal pair of projection centers of the Steiner conic, thereby obtaining the corresponding vanishing lines and images of circular points. Finally, the five camera parameters are fully calibrated using images of circular points obtained from at least three images. We summarize our contributions as follows:

1. We find that a new fixed line can be obtained from the image, which is an invariant under general motion;
2. New constraints are derived from the general eigenvectors of the image of the absolute conic and the Steiner conic for calibrating the three intrinsic parameters of the camera;
3. We obtain the optimal pair of projection centers of the Steiner conic for fully calibrating all five intrinsic parameters of the camera, and our method achieves state-of-the-art accuracy for auto-calibration under general motion.

The paper is organized as follows. Section 2 introduces some basic concepts that will be used in the following sections. Section 3 proposes a method for determining a fixed line under general motion. Section 3 and 4 describe the two properties of the fixed line and the derived calibration method, respectively. Section 5 lists the degenerate cases. Synthetic and real experiments on the proposed method are shown in Section 6. Conclusions are given in Section 7.

2 Preliminary

This section briefly introduces the basic concepts that will be used for camera calibration. We use a pinhole camera model to represent camera intrinsics.

2.1 The pinhole camera model

A 3D point $\mathbf{P} = [X, Y, Z, 1]^T$ is projected into the image at $\mathbf{p} = [u, v, 1]^T$ by

$$\mu\mathbf{p} = \mathbf{K}\,[\mathbf{R}|\mathbf{t}]\,\mathbf{P}, \tag{1}$$

where μ is a non-zero scalar, $[\mathbf{R}|\mathbf{t}]$ denotes the rigid body transformation, and $\mathbf{K}$ is the camera intrinsic matrix, as

$$\mathbf{K} = \begin{bmatrix} f_x & s & u_0 \\ 0 & f_y & v_0 \\ 0 & 0 & 1 \end{bmatrix}. \tag{2}$$

Here f_x and f_y are the focal lengths along x- and y-*axis*, respectively. s is the skew parameter, $(u_0,\, v_0)$ is the principal point.

The absolute conic is a conic at infinity [13], which is projected into the image of the absolute conic (IAC) $\boldsymbol{\omega} = \mathbf{K}^{-T}\mathbf{K}^{-1}$, whose dual is $\boldsymbol{\omega}^* = \mathbf{K}\mathbf{K}^T$. Once at least five independent constraints on $\boldsymbol{\omega}$ is obtained, the intrinsic matrix $\mathbf{K}$ can be determined by the Cholesky decomposition [13], [9] of $\boldsymbol{\omega}$.

2.2 The Steiner conic from the fundamental matrix

The fundamental matrix $\mathbf{F}$ can be decomposed into a symmetric part $\mathbf{F}_s$ and a skew-symmetric part $\mathbf{F}_a$ [13], i.e.,

$$\mathbf{F}_s = \frac{\mathbf{F} + \mathbf{F}^T}{2}, \quad \mathbf{F}_a = \frac{\mathbf{F} - \mathbf{F}^T}{2}, \tag{3}$$

so that $\mathbf{F} = \mathbf{F}_s + \mathbf{F}_a$. Geometrically, $\mathbf{F}_s$ is a Steiner conic, which is the image of the horopter curve ($\mathbf{x} = \mathbf{x}'$) formed by a series of intersection points $\mathbf{x}_c$ of the corresponding epipolar lines $\mathbf{l}$ and $\mathbf{l}'$ in the two views (see Fig. 1).

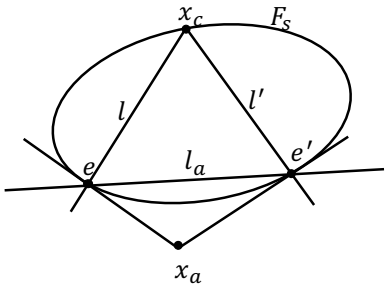

Fig. 1. Geometric representation F. The fundamental matrix $\mathbf{F}$ is decomposed into a symmetric part $\mathbf{F}_s$ and a skew-symmetric part $\mathbf{F}_a$. Under general motion, $\mathbf{F}_s$ is the Steiner conic formed by the horopter points $\mathbf{x}_c$, which are the intersections of the corresponding epipolar lines $\{\mathbf{l}, \mathbf{l}'\}$ in the two views. The line $\mathbf{l}_a$ is polar of $\mathbf{x}_a$, the null-vector of $\mathbf{F}_a$, and intersects $\mathbf{F}_s$ at the epipoles $\mathbf{e}, \mathbf{e}'$ of the two views.

$\mathbf{F}_a$ can be written as $\mathbf{F}_a = [\mathbf{x}_a]_\times$, where the point $\mathbf{x}_a$ is the null-vector of $\mathbf{F}_a$. The polar of $\mathbf{x}_a$ with respect to $\mathbf{F}_s$ is the line $\mathbf{l}_a = \mathbf{F}_s\mathbf{x}_a$, intersects with $\mathbf{F}_s$ at the two epipoles $\{\mathbf{e}, \mathbf{e}'\}$, i.e., $\mathbf{l}_a = \mathbf{e} \times \mathbf{e}'$. Here $\mathbf{e}$ and $\mathbf{e}'$ are the null vectors of $\mathbf{F}$ and $\mathbf{F}^T$, respectively. Consequently, once $\mathbf{F}$ is determined by the normalized eight-point algorithms [13] or the five-point method [3], $\mathbf{F}_s$, the epipoles $\{\mathbf{e}, \mathbf{e}'\}$, the skew-symmetric point $\mathbf{x}_a$ and its polar $\mathbf{l}_a$ can be uniquely defined.

3 The fixed line and camera calibration

This section introduces a fixed line and its property, which can be used for camera calibration. For a pair of views under general motion, let $\mathbf{v}_\perp = \boldsymbol{\omega}^*\mathbf{l}_a$ is

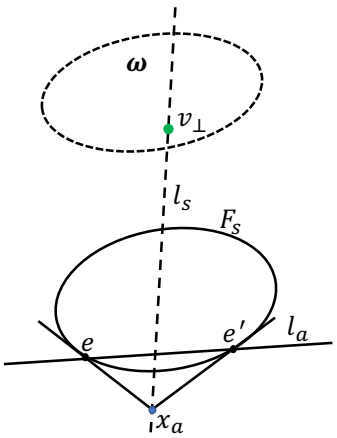

Fig. 2. The fixed line $\mathbf{l}_s$ of two views under general motion. The point $\mathbf{v}_\perp$ is the pole of the line $\mathbf{l}_a$ w.r.t the IAC $\boldsymbol{\omega}$. The lines $\mathbf{l}_s$ and $\mathbf{l}_a$ are orthogonal with respect to $\boldsymbol{\omega}$, where the line $\mathbf{l}_s$ is obtained by connecting the points $\mathbf{v}_\perp$ and $\mathbf{x}_a$.

the pole of the line $\mathbf{l}_a$ with respect to the IAC $\boldsymbol{\omega}$, the line $\mathbf{l}_s$ (see Fig. 2) be the fixed line connecting the points $\mathbf{x}_a$ and $\mathbf{v}_\perp$, as

$$\begin{aligned} \mathbf{l}_s &= \mathbf{x}_a \times \mathbf{v}_\perp \\ &= \left[\mathbf{x}_a\right]_\times \mathbf{v}_\perp \\ &= \mathbf{F}_a \boldsymbol{\omega}^* \mathbf{l}_a. \end{aligned} \tag{4}$$

As $\mathbf{F}_a$ is skew-symmetric, left-multiplying $\mathbf{l}_a^T \boldsymbol{\omega}^*$ on both sides of Eq. 4, we obtain

$$\mathbf{l}_a^T \boldsymbol{\omega}^* \mathbf{l}_s = \mathbf{l}_a^T \boldsymbol{\omega}^* \mathbf{F}_a \boldsymbol{\omega}^* \mathbf{l}_a = 0. \tag{5}$$

Hence the lines $\mathbf{l}_a$ and $\mathbf{l}_s$ are orthogonal with respect to $\boldsymbol{\omega}$, where $\mathbf{l}_s$ and $\mathbf{l}_a$ can be regarded as the vanishing lines of two perpendicular planes in 3D space [13].

3.1 General eigenvectors of IAC $\boldsymbol{\omega}$ and $\mathbf{F}_s$

Here we introduce the location of general eigenvectors of IAC $\boldsymbol{\omega}$ and $\mathbf{F}_s$.

Proposition 1. *Under general motion, one of the general eigenvectors of the IAC $\boldsymbol{\omega}$ and Steiner conic $\mathbf{F}_s$ lies on the line $\boldsymbol{l}_a$, and the other two are on $\boldsymbol{l}_s$.*

Proof. For two views captured by the same camera under general motion, the IAC $\boldsymbol{\omega}$ and the Steiner conic $\mathbf{F}_s$ can be drawn as two separated conics (see Fig. 3). Inspired by [13], [15], [14], [29], there is a unique common self-polar triangle $\triangle \mathbf{v}_1 \mathbf{v}_2 \mathbf{v}_3$ with respect to these two conics, whose vertices are the general eigenvectors of $\boldsymbol{\omega}^* \mathbf{F}_s$, as

$$\mathbf{F}_s \mathbf{v}_i \sim \boldsymbol{\omega} \mathbf{v}_i \Rightarrow \left(\boldsymbol{\omega}^* \mathbf{F}_s - \gamma_i \mathbf{I}\right) \mathbf{v}_i = \mathbf{0}_{3\times 1}, \tag{6}$$

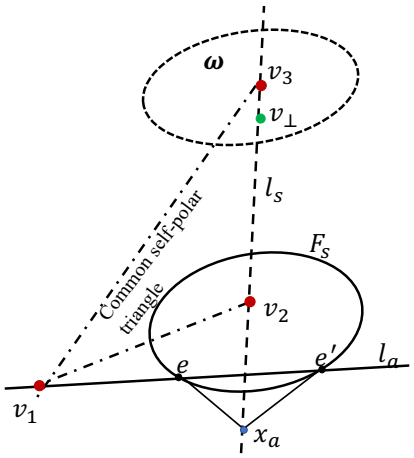

Fig. 3. Location of the general eigenvectors of the IAC $\boldsymbol{\omega}$ and the Steiner conic $\mathbf{F}_s$. Under general motion, the IAC $\boldsymbol{\omega}$ and Steiner conic $\mathbf{F}_s$ can be drawn as two fixed but separate conics. There is only one common self-polar triangle $\triangle\mathbf{v}_1\mathbf{v}_2\mathbf{v}_3$, whose vertices are the general eigenvectors of $\boldsymbol{\omega}^*\mathbf{F}_s$. The general eigenvector $\mathbf{v}_1$ is on the line $\mathbf{l}_a$. The other two, $\mathbf{v}_2$ and $\mathbf{v}_3$, lie on the fixed line $\mathbf{l}_s$.

where γ_i is the non-zero eigenvalues with $i = 1$, 2, and 3. As demonstrated in [15], [14], the position of $\triangle\mathbf{v}_1\mathbf{v}_2\mathbf{v}_3$ is fixed with respect to the two conics. The vertex $\mathbf{v}_1$ locates apart from the two conics, and the other two vertices $\mathbf{v}_2$ and $\mathbf{v}_3$ are located inside the two conics, respectively. In addition, based on the pole-polar relationship, the general eigenvectors $(\mathbf{v}_1, \mathbf{v}_2, \mathbf{v}_3)$ satisfy with

$$\begin{cases} \mathbf{v}_i \sim \mathbf{F}_s^{-1}\left(\mathbf{v}_j \times \mathbf{v}_k\right), & \text{(7a)} \\ \mathbf{v}_i \sim \boldsymbol{\omega}^*\left(\mathbf{v}_j \times \mathbf{v}_k\right), & \text{(7b)} \end{cases}$$

where $\{i, j, k\} = \{1, 2, 3\}$. Let $\mathbf{l}_v$ be the line joining $\mathbf{v}_2$ and $\mathbf{v}_3$, $\mathbf{v}_\perp$ satisfies with

$$\begin{aligned} \mathbf{v}_\perp^T\mathbf{l}_v &\sim \mathbf{v}_\perp^T\left(\mathbf{v}_2 \times \mathbf{v}_3\right) \\ &\sim \mathbf{v}_\perp^T\mathbf{F}_s\mathbf{F}_s^{-1}\left(\mathbf{v}_2 \times \mathbf{v}_3\right) \\ &\sim \mathbf{l}_a^T\boldsymbol{\omega}^*\mathbf{F}_s\mathbf{v}_1 \\ &\sim \mathbf{l}_a^T\mathbf{v}_1. \end{aligned} \tag{8}$$

And from Eq. 7, the point $\mathbf{x}_a = \mathbf{F}_s^{-1}\mathbf{l}_a$ satisfies

$$\begin{aligned} \mathbf{x}_a^T\mathbf{l}_v &\sim \left(\mathbf{F}_s^{-1}\mathbf{l}_a\right)^T\left(\mathbf{v}_2 \times \mathbf{v}_3\right) \\ &\sim \left(\mathbf{F}_s^{-1}\mathbf{l}_a\right)^T\boldsymbol{\omega}\boldsymbol{\omega}^*\left(\mathbf{v}_2 \times \mathbf{v}_3\right) \\ &\sim \mathbf{l}_a^T\mathbf{F}_s^{-1}\boldsymbol{\omega}\mathbf{v}_1 \\ &\sim \mathbf{l}_a^T\mathbf{v}_1. \end{aligned} \tag{9}$$

From Eq. 8 and 9, we can have $\mathbf{x}_a^T \mathbf{l}_v = \kappa \mathbf{v}_\perp^T \mathbf{l}_v \Rightarrow \left(\mathbf{x}_a^T - \kappa \mathbf{v}_\perp^T\right) \mathbf{l}_v = 0$, where κ is a non-zero scalar. Hence, the line $\mathbf{l}_s$ connecting $\mathbf{x}_a$ and $\mathbf{v}_\perp$ aligns with the line $\mathbf{l}_v$, thus both $\mathbf{v}_2$ and $\mathbf{v}_3$ lies on $\mathbf{l}_s$, i.e., $\mathbf{l}_s \sim \mathbf{v}_2 \times \mathbf{v}_3$. Furthermore, it can be easily derived that $\mathbf{l}_a^T \mathbf{v}_1 \sim \mathbf{x}_a^T \mathbf{l}_s = 0$, which indicates the eigenvector $\mathbf{v}_1$ lies on $\mathbf{l}_a$. □

3.2 Calibration of the focal lengths and the skew

In order to eliminate the unknown eigenvalues γ_i in Eq. 6, we can substitute the skew-symmetric matrix of the corresponding eigenvectors on both sides of the equation. Furthermore, since the general eigenvector $\mathbf{v}_1$ lies on the line $\mathbf{l}_a$, the constraints on the IAC $\boldsymbol{\omega}$ for calibrating the camera can be obtained as

$$\begin{cases} \mathbf{l}_a^T \mathbf{v}_1 = 0, & \text{(10a)} \\ [\mathbf{v}_1]_\times \boldsymbol{\omega}^* \mathbf{F}_s \mathbf{v}_1 = \mathbf{0}_{3\times 1}, & \text{(10b)} \end{cases}$$

which include three independent constraints. Let $\mathbf{v}_1$ have two unknown coordinates (v_{1x}, v_{1y}) and the camera have only one unknown focal length f. The three unknowns, i.e., f, v_{1x}, and v_{1y}, can therefore be uniquely recovered by solving Eq. 10. Furthermore, for a camera with the known principal point, the focal length (f_x, f_y), skew s, and six parameters of three distinct $\mathbf{v}_1$ for each pair of views can be recovered through the nine independent constraints (Eq. 10) that are obtained from three images.

4 Full calibration using the centers of the Steiner conic

This section presents the properties of the centers of the Steiner conic $\mathbf{F}_s$ and then introduces a method to calibrate all the five camera intrinsic parameters.

4.1 The centers of the Steiner conic $\mathbf{F}_s$

Proposition 2. *Suppose the Steiner conic $\boldsymbol{F}_s$ is the projection of a circle on the image plane. Its two projected centers $\boldsymbol{o}_{1,2}$ are associated with two opposite viewing directions of $\boldsymbol{F}_s$, both lying on the fixed line $\boldsymbol{l}_s$. They correspond to the two planes containing the circle. Furthermore, the general eigenvector $\boldsymbol{v}_1$, which lies outside the two conic $\boldsymbol{F}_s$ and $\boldsymbol{\omega}$ coincides with the intersection of the vanishing lines of these two planes $\boldsymbol{l}_{h1,2}$.*

Proof. In projective geometry, any non-degenerate conic is projectively equivalent to a circle [13]. Therefore, based on different viewing directions, there are two projected centers of the Steiner conic $\mathbf{F}_s$ [13], [29]. One is along the camera's viewing direction, and the other is on the opposite viewing direction. Inspired by [35], [24], [15], [14], IAC $\boldsymbol{\omega}$ and the Steiner conic $\mathbf{F}_s$ intersect at four distinct circular points $\mathbf{i}_i, \mathbf{j}_i$, forming two vanishing lines $\mathbf{l}_{hi}$ as (see Fig. 4 (a))

$$\mathbf{l}_{hi} = \mathbf{i}_i \times \mathbf{j}_i, \tag{11}$$

where $i = 1, 2$. The two pairs of circular points form a quadrangle, $\mathbf{i}_1\mathbf{i}_2\mathbf{j}_1\mathbf{j}_2$ (see Fig. 4 (b)). The diagonal triangle $\triangle\mathbf{v}_1\mathbf{v}_2\mathbf{v}_3$ is self-polar triangle for the IAC $\boldsymbol{\omega}$ [13] [14], where the point $\mathbf{v}_1$ is the intersection point of the diagonals of the quadrangle, and the points $\mathbf{v}_2$ and $\mathbf{v}_3$ are the intersection of two opposite sides of the quadrilateral. Therefore, we can get $\mathbf{v}_1 = \mathbf{l}_{h1} \times \mathbf{l}_{h2}$.

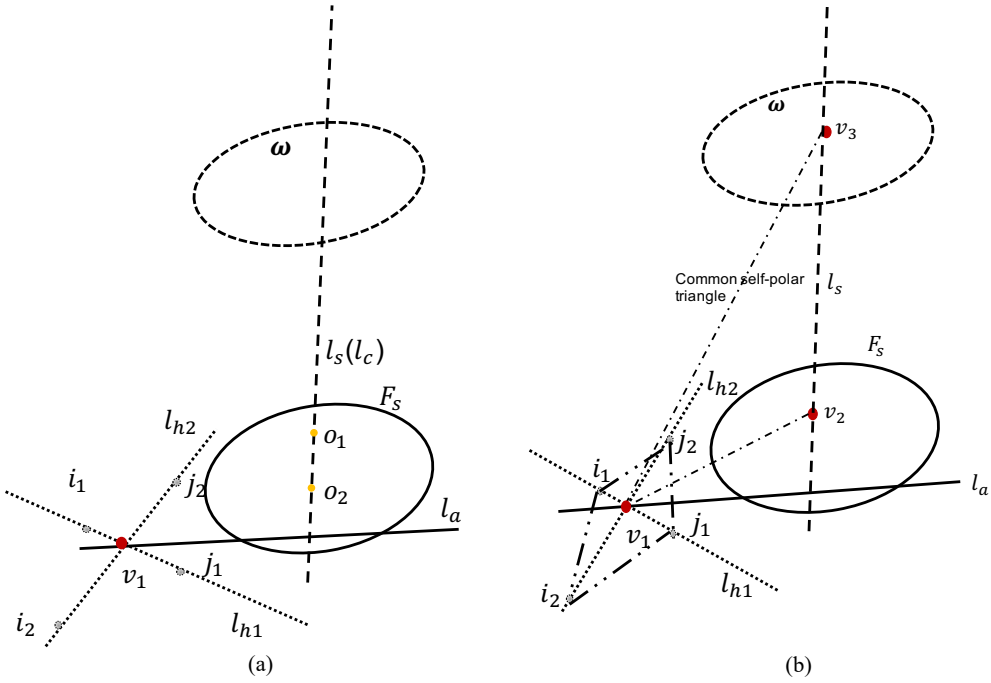

Fig. 4. The projected centers of Steiner conic $\mathbf{F}_s$ are on the line $\mathbf{l}_s$. (a) The intersection points of IAC $\boldsymbol{\omega}$ and the Steiner conic $\mathbf{F}_s$ are two pairs of circular points $\mathbf{i}_i, \mathbf{j}_i$, and form two vanishing lines $\mathbf{l}_{hi}$, where $i = 1, 2$. Accordingly, based on the pole-polar relationship with respect to $\mathbf{F}_s$, two projected centers $\mathbf{o}_i$ associated with $\mathbf{l}_{hi}$ and lie on the line $\mathbf{l}_s$. (b) The general eigenvector $\mathbf{v}_1$, which lies outside the two conics $\mathbf{F}_s$ and $\boldsymbol{\omega}$, coincides with the intersection of the two vanishing lines $\mathbf{l}_{hi}$.

According to the pole-polar relationship, these two projected centers of $\mathbf{F}_s$ can be obtained by $\mathbf{o}_i \sim \mathbf{F}_s^{-1}\mathbf{l}_{hi}$, which form a line $\mathbf{l}_c$ as

$$\begin{aligned} \mathbf{l}_c &\sim \mathbf{o}_1 \times \mathbf{o}_2 \\ &\sim \mathbf{F}_s^{-1}\mathbf{l}_{h1} \times \mathbf{F}_s^{-1}\mathbf{l}_{h2} \\ &\sim (\mathbf{F}_s^{-1})^*(\mathbf{l}_{h1} \times \mathbf{l}_{h2}) \\ &\sim \mathbf{F}_s\mathbf{v}_1. \end{aligned} \tag{12}$$

From Proposition 1, we can get $\mathbf{l}_s \sim \mathbf{l}_c \sim \mathbf{o}_1 \times \mathbf{o}_2$.

□

Therefore, once the projected centers $\mathbf{o}_i$ of the Steiner conic $\mathbf{F}_s$ are obtained, the polar lines $\mathbf{l}_{hi}$ with respect to $\mathbf{F}_s$ can be recovered. They intersect $\mathbf{F}_s$ at two pairs of circular points $\mathbf{i}_i$, $\mathbf{j}_i$, which lie on the image of the absolute conic $\boldsymbol{\omega}$ as

$$\mathbf{i}_i^T \boldsymbol{\omega} \mathbf{i}_i = \mathbf{j}_i^T \boldsymbol{\omega} \mathbf{j}_i = 0. \tag{13}$$

4.2 Recovery of the centers of the Steiner conic $\mathbf{F}_s$

When the principal point is known, Section 3.2 introduces a method to calibrate three camera intrinsic parameters using three views. When the principal point is unknown, it is theoretically possible to fully recover the camera intrinsic parameters using the method in Section 3.2. However, due to the high order of ambiguity, full camera calibration is not easy to achieve [13]. Instead, as described in Section 4.1, the intersection of the IAC $\boldsymbol{\omega}$ and the Steiner conic $\mathbf{F}_s$ are two pairs of imaged circular points, which provide four linear orthogonal constraints on IAC $\boldsymbol{\omega}$ (Eq. 13). Therefore, from three views, six pairs of imaged circular points are sufficient to calibrate the five camera intrinsic parameters.

Taking the center of the image as the initial value of the principal point, we can first get the initial focal length $\hat{f}_x$, $\hat{f}_y$, the skew $\hat{s}$ from three images, using the method in Section 3.2, and thus the initial IAC $\hat{\boldsymbol{\omega}}$. For any two views, the image of circular points $\hat{\mathbf{i}}_i, \hat{\mathbf{j}}_i$ can be found by intersecting the initial $\hat{\boldsymbol{\omega}}$ with $\mathbf{F}_s$, so as the vanishing lines $\hat{\mathbf{l}}_{hi}$, by connecting the $\hat{\mathbf{i}}_i, \hat{\mathbf{j}}_i$, respectively. The two initial projected centers $\hat{\mathbf{o}}_i$ of $\mathbf{F}_s$ can then be recovered by $\hat{\mathbf{o}}_i = \mathbf{F}_s^{-1} \hat{\mathbf{l}}_{hi}$ (i = 1, 2).

Next, we set the search range for the optimal solution centered on the two initial centers $\hat{\mathbf{o}}_i$. We generate a series of uniformly distributed sample points within these ranges. For each pair of the sample points $\tilde{\mathbf{o}}_i$, we can get the line $\tilde{\mathbf{l}}_s = \tilde{\mathbf{o}}_1 \times \tilde{\mathbf{o}}_2$. We can also get the corresponding vanishing line $\tilde{\mathbf{l}}_{hi}$ using the pole-polar relationship $\tilde{\mathbf{l}}_{hi} = \mathbf{F}_s \tilde{\mathbf{o}}_i$ with respect to $\mathbf{F}_s$. Then, we can calculate the new imaged circular points $\tilde{\mathbf{i}}_i, \tilde{\mathbf{j}}_i$, which are the intersections of the vanishing line $\tilde{\mathbf{l}}_{hi}$ and $\mathbf{F}_s$. We then use Eq. 13 to recover the corresponding image of the absolute conic $\tilde{\boldsymbol{\omega}}$. Finally, all the obtained parameters, the conic centers $\tilde{\mathbf{o}}_i$, the image of circular points $\tilde{\mathbf{i}}_i, \tilde{\mathbf{j}}_i$, the corresponding IAC $\tilde{\boldsymbol{\omega}}$, the Steiner conics $\mathbf{F}_s$, the lines $\mathbf{l}_a$, and the points $\mathbf{x}_a$, are regarded as the input value to substitute into the *cost function* for an iterative optimization.

According to the properties of the line $\mathbf{l}_s$ and its Euclidean geometry property, our cost function for the optimal conic centers $\tilde{\mathbf{o}}_i$ by the Levenberg-Marquardt optimization [27] is

$$cost = \sum_{3}^{N} (\tilde{\mathbf{l}}_s^T \tilde{\boldsymbol{\omega}}^* \mathbf{l}_a + \tilde{\mathbf{l}}_s^T \mathbf{x}_a + \mathbf{l}_l^T \tilde{\boldsymbol{\omega}}^* \mathbf{l}_r), \tag{14}$$

where N is the number of images. $\tilde{\mathbf{l}}_s^T \tilde{\boldsymbol{\omega}}^* \mathbf{l}_a$ contains the orthogonality between $\tilde{\mathbf{l}}_s$ and $\mathbf{l}_a$, where $\tilde{\mathbf{l}}_s$ is obtained by connecting the two center $\tilde{\mathbf{o}}_i$. $\tilde{\mathbf{l}}_s^T \mathbf{x}_a$ indicates $\tilde{\mathbf{l}}_s$ defined by the projected centers of $\mathbf{F}_s$ should also pass through the fixed point

$\mathbf{x}_a$. $\mathbf{l}_l^T \tilde{\boldsymbol{\omega}}^* \mathbf{l}_r$ contains the orthogonality between the lines $\mathbf{l}_l$ and $\mathbf{l}_r$ (see Fig. 5) since $\tilde{\mathbf{l}}_s$ passes through the two centers of the conic $\mathbf{F}_s$. Let $\mathbf{x}_c$ be an arbitrary point on $\mathbf{F}_s$, $\mathbf{l}_l = \mathbf{p}_1 \times \mathbf{x}_c$, $\mathbf{l}_r = \mathbf{p}_2 \times \mathbf{x}_c$, where the point $\mathbf{p}_1$ and $\mathbf{p}_2$ are the image of the terminal vertexes of the diameter and can be obtained as the intersections of the line $\tilde{\mathbf{l}}_s$ and $\mathbf{F}_s$.

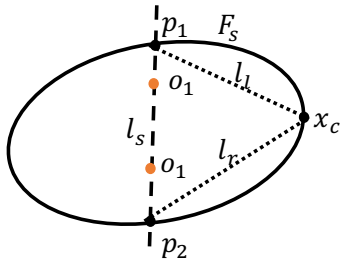

Fig. 5. The illustration for $\mathbf{l}_l^T \tilde{\boldsymbol{\omega}}^* \mathbf{l}_r$. The points $\mathbf{p}_1$ and $\mathbf{p}_2$ are the intersections of $\mathbf{l}_s$ and $\mathbf{F}_s$, and are also the endpoints of the diameter. $\mathbf{x}_c$ is an arbitrary point on $\mathbf{F}_s$. The lines $\mathbf{l}_l$ and $\mathbf{l}_r$ are formed by connecting $\mathbf{x}_c$ with $\mathbf{p}_1$ and $\mathbf{p}_2$, respectively. Moreover, hence $\mathbf{l}_l^T \tilde{\boldsymbol{\omega}}^* \mathbf{l}_r$ contains the orthogonality between the lines $\mathbf{l}_l$ and $\mathbf{l}_r$.

Once the iterative optimization converges, we can obtain three pairs of optimized conic centers $\mathbf{o}_i$. Based on the pole-polar relationship, the corresponding vanishing lines $\mathbf{l}_{hi}$ can be recovered with the optimized conic centers $\mathbf{o}_i$ with respect to the Steiner conic $\mathbf{F}_s$, i.e., $\mathbf{l}_{hi} = \mathbf{F}_s \mathbf{o}_i$, and then further obtain the pairs of the image of circular points $\mathbf{i}_i, \mathbf{j}_i$. The IAC $\boldsymbol{\omega}$ with five unknown parameters can be recovered from three or more images by the linear orthogonality constraint in Eq. 13. Finally, the intrinsic matrix $\mathbf{K}$ can be obtained through Cholesky decomposition on the IAC $\boldsymbol{\omega}$ [9].

5 Degenerate cases

The proposed method cannot be used for camera calibration when the camera performs degenerate motions such as pure translation, rotation, and planar motion. Because in these cases, although the point $\mathbf{x}_a$ and its polar line $\mathbf{l}_a$ can be recovered from $\mathbf{F}_s$, $\mathbf{F}_s$ is degenerate, and we cannot recover the complete Steiner conic to get the image of the circular points. Another work will be carried out to introduce detailed camera calibration methods for degenerate motion using different constraints.

6 Experiments and results

Experiments are carried out on synthetic and real data to evaluate the feasibility of the proposed methods.

6.1 Synthetic data

In synthetic experiments, a cube mesh containing 3000 3D points (see Fig. 6) was projected into images using predefined projection matrices. Image size is 520 × 480. The camera focal lengths are $f_x = 1000$, $f_y = 800$, the skew is $s = 0.1$, and the principal point is $(u_0, v_0) = (270, 250)$. The external parameters of general motion are randomly set. We add 0 to 3 pixels of uniform random noise to each image point with a noise step size of 0.1. For each noise level, 100 independent trials were conducted to evaluate the feasibility of the proposed method.

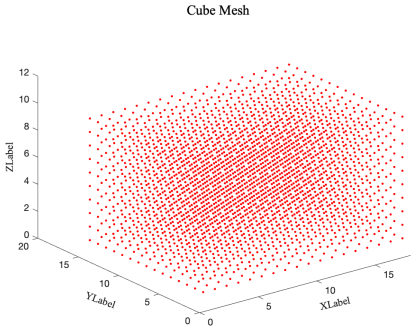

Fig. 6. The synthetic object is a cube mesh containing 3000 3D points.

Known Principal Point. The camera is calibrated from three images using the method described in Section 3.2, with the known principal point. Fig. 7 shows the results of calibrated focal length f_x, f_y and the skew s versus different image noise levels. It can be seen that the medians of the three calibrated parameters are accurate, all close to the ground truth. The relative errors at noise level 1.0 are $f_x = 0.02\%$, $f_y = 0.17\%$. Since the scale of the skew s is much smaller than that of the focal length, its direct estimation tends to be unstable. However, the errors of skew angle θ in $s = -f_x \cot\theta$ [7] is less than 0.2° (0.017%) compared to the ground truth angle.

Full Camera Auto-Calibration. In this case, the camera is first calibrated from three images using the method described in Section 3.2, assuming the initial principal point is at the center of the image. The pair of projected centers of the Steiner conic are then initialized and used to set the searching ranges for optimal solutions using the methods described in Section 4.2. In each searching range, 100 uniformly distributed sample image points are generated. Finally, the five camera intrinsic parameters are fully calibrated. Fig. 8 shows the results of calibrated focal length f_x, f_y, u_0, v_0 and the skew s versus different image noise levels. It can be seen that the medians of the calibrated parameters are accurate, all close to the ground truth. The relative errors at noise level 1.0 are

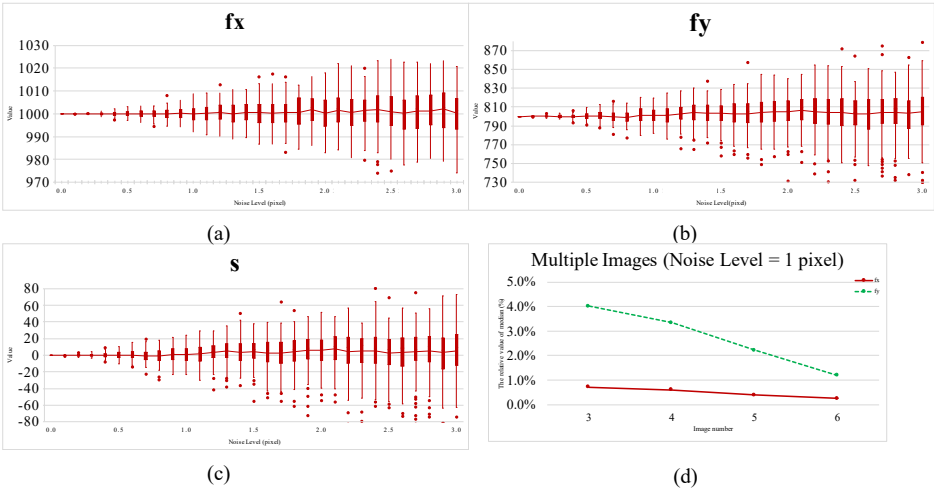

Fig. 7. (a) - (c) Boxplots of known principal points, calibrated focal length f_x, f_y and skew s under different image noise levels. (d) The relative errors of the calibrated focal length f_x and f_y with respect to the number of images under the noise level 1.0.

$f_x = 0.13\%$, $f_y = 0.33\%$, $u_0 = 2.35\%$, and $v_0 = 4.01\%$. The errors of skew angle θ in $s = -f_x \cot\theta$ is less than 0.9° (1.0%) compared to the ground truth angle.

Furthermore, the estimate of skew s in this case is worse than when the principal points are known. In addition to the scale issue we mentioned earlier, in this case the instability of the principal point here makes f_y worse, further affecting the skewed s estimate. Fortunately, we can adopy the general zero skew s assumption to provide more stable calibration results [25], [8], [13], [36].

Increased Number of Images. As mentioned in [36], the error decreases when more images are used. At noise level 1.0, we use more images to verify the accuracy of the camera calibration for three (see Fig. 7 (d)) or five parameters (Fig. 8 (f)), respectively. The median value of each obtained camera parameter is regarded as the best result. As can be seen from Fig. 7 (d) and Fig. 8 (f), the relative error of the camera intrinsic parameters decreases as the number of images increases. For both cases, an optimal result can be obtained when at least six images are used.

6.2 Real scenes

In the real experiment, a set of images is captured by Nikon D300s with the image size 4032×3024. The ground truth is obtained as the calibration results of the chessboard method [36] from 12 images.

Known Principal Point. The Nikon D300s is calibrated with 3, 6, 10 images respectively, using the image center as the principal point. The calibration results of focal length f_x, f_y and skew s are shown in Table 1. It can be seen that our

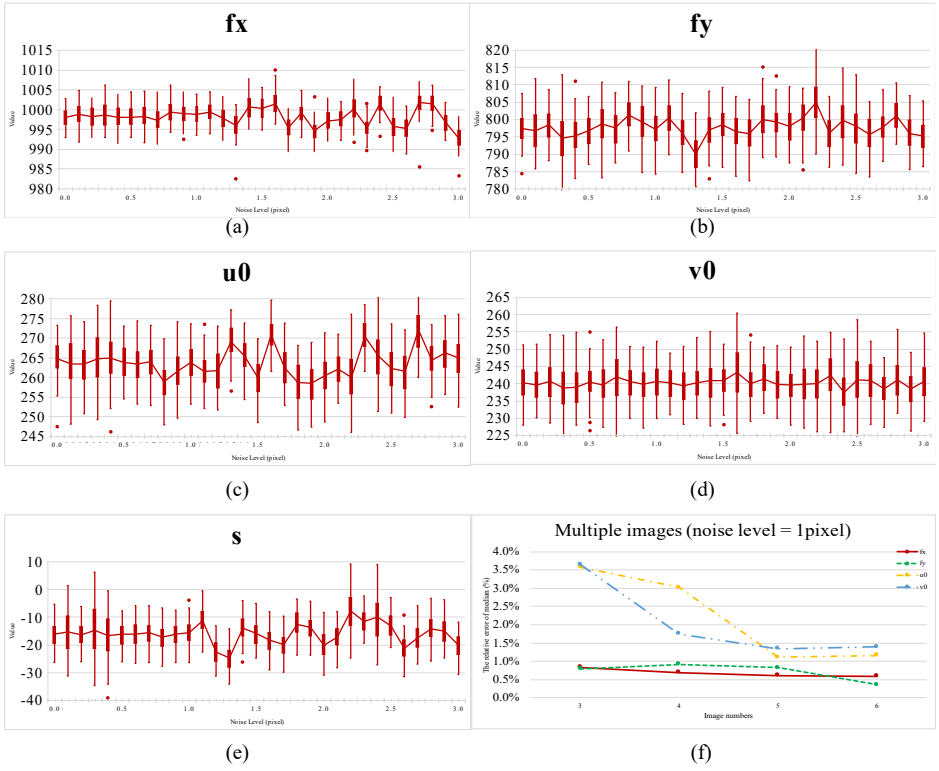

Fig. 8. (a) - (e) Boxplots of calibrated focal length f_x, f_y, principal point u_0, v_0 and skew s under different image noise levels. (f) The relative errors of the calibrated focal length f_x, f_y, and principal point u_0, v_0 with respect to the number of images under the noise level 1.0.

method can obtain accurate focal length calibration results, and the relative error of focal length is about 4%. The skew s is not accurately estimated, but can be assumed to be zero to provide more stable calibration results. Meanwhile, as more images are used in the calibration, the relative error decreases.

Full camera auto-calibration of intrinsic parameters. Using the method in Sec. 4.2, we fully calibrate five camera intrinsic parameters with 3, 6, 10 images, respectively. We also provide a comparison with the widely used auto-calibration method GA-PSO [21] and the results are shown in Table 2. It can be seen that the relative errors achieve better accuracy compared with GA-PSO. The skew s is not accurately estimated, but can be assumed to be zero to provide more stable calibration results [8]. Meanwhile, as more images are used in the calibration, the relative error decreases.

Table 1. Results with the known principal point.

Methods	f_x	f_y	s
GT (12 images) [36]	4486.74	4493.00	-4.07
Ours (3 images)	4213.02 (6.10%)	4722.08 (5.10%)	57.20
Ours (6 images)	4703.82 (4.84%)	4291.95 (4.48%)	-46.40
Ours (10 images)	4692.24 (4.58%)	4301.74 (4.25%)	-12.46

Table 2. Results of full auto-calibration of intrinsic parameters.

Methods	f_x	f_y	s	u_0	v_0
GT(12)	4486.70	4493.00	-4.07	2162.40	1464.70
GA-PSO(3)	4073.27 (9.22%)	4059.92 (9.63%)	251.13	1944.27 (10.08%)	1278.97 (12.68%)
Ours(3)	4287.14 (4.45%)	4234.33 (5.76%)	172.72	2005.88 (7.24%)	1334.47 (8.89%)
GA-PSO(6)	4252.29 (5.22%)	4171.24 (7.16%)	148.49	2389.43 (10.50%)	1319.74 (9.90%)
Ours(6)	4343.96 (3.18%)	4730.33 (5.28%)	142.68	2019.71 (6.60%)	1380.54 (5.75%)
GA-PSO(10)	4699.22(4.74%)	4234.33 (5.76%)	104.05	1990.95 (7.92%)	1354.28 (7.53%)
Ours(10)	4333.79 (3.41%)	4678.82 (4.14%)	108.62	2050.43 (5.18%)	1391.40 (5.01%)

7 Conclusions

This paper proposes new constraints derived from the Steiner conic, the symmetric part of the fundamental matrix, to solve the problem of camera auto-calibration. A method has been presented to determine a fixed line between two views under general motion. We then introduced and proved two properties of the fixed line that can be used for calibration. Based on a known principal point and the new constraints, we presented a method that can calibrate the focal lengths and the skew from three images. Moreover, we proposed a method to fully calibrate the five camera intrinsic parameters through iterative optimization from at least three images, by recovering the pair of the projected centers of the Steiner conic. Finally, we verified the feasibility and accuracy of the proposed method through synthetic and real experiments and achieved state-of-the-art calibration results.

Acknowledgement. This work was supported by the National Key Research and Development Program of China (2022YFE0201400), the National Natural Science Foundation of China (62076029), Guangdong Science and Technology Department (2022B1212010006, 2017A030313362) and internal funds of the United International College (R202012, R201802, UICR0400025-21).

References

1. Agapito, L., Hartley, R., Hayman, E.: Linear calibration of a rotating and zooming camera (1999)
2. Agapito, L., Hayman, E., Reid, I.D.: Self-calibration of rotating and zooming cameras. International Journal of Computer Vision **47**, 287 (2005)

3. Barath, D.: Five-point fundamental matrix estimation for uncalibrated cameras. 2018 IEEE/CVF Conference on Computer Vision and Pattern Recognition pp. 235–243 (2018)
4. Chen, H.Y., Matsumoto, K., Ota, J., Arai, T.: Self-calibration of environmental camera for mobile robot navigation. Robotics and Autonomous Systems **55**, 177–190 (2007)
5. Dyer, C.R.: Volumetric scene reconstruction from multiple views. In: Foundations of Image Understanding. pp. 469–489. Kluwer (2001)
6. Espuny, F.: A new linear method for camera self-calibration with planar motion. Journal of Mathematical Imaging and Vision **27**, 81–88 (2006)
7. Faugeras, O.D., Luong, Q., Maybank, S.J.: Camera self-calibration: Theory and experiments pp. 321–334 (1992)
8. Fetzer, T., Reis, G., Stricker, D.: Stable intrinsic auto-calibration from fundamental matrices of devices with uncorrelated camera parameters. 2020 IEEE Winter Conference on Applications of Computer Vision (WACV) pp. 221–230 (2020)
9. Gentle, J.: Numerical linear algebra for applications in statistics (1998)
10. Gurdjos, P., Sturm, S., Wu, Y.H.: Euclidean structure from n $\geq$ 2 parallel circles: Theory and algorithms pp. 238 – 252 (2006)
11. Habed, A., Boufama, B.: Camera self-calibration from triplets of images using bivariate polynomials derived from kruppa's equations. IEEE International Conference on Image Processing 2005 **2**, II–1174 (2005)
12. Hartley, R.: Kruppa's equations derived from the fundamental matrix. IEEE Transactions on Pattern Analysis and Machine Intelligence **19**, 133–135 (1997)
13. Hartley, R., Zisserman, A.: Multiple view geometry in computer vision. Cambridge University Press, second edn. (2003)
14. Huang, H.F., Zhang, H., Cheung, Y.M.: The common self-polar triangle of separate circles: Properties and applications to camera calibration. 2016 IEEE International Conference on Image Processing (ICIP) pp. 1170–1174 (2016)
15. Huang, H.F., Zhang, H., Cheung, Y.M.: Homography estimation from the common self-polar triangle of separate ellipses. 2016 IEEE Conference on Computer Vision and Pattern Recognition (CVPR) pp. 1737–1744 (2016)
16. Jaynes, C.: Multi-view calibration from planar motion trajectories. Image Vis. Comput. **22**, 535–550 (2004)
17. Ji, Q., Zhang, Y.M.: Camera calibration with genetic algorithms. IEEE Transactions on Systems, Man, and Cybernetics - Part A: Systems and Humans **31**, 120–130 (2001)
18. Jiang, Z.T., Wu, W.H., Wu, M.: Camera autocalibration from kruppa's equations using particle swarm optimization. In: CSSE (2008)
19. Koch, R., Gool, L.V.: 3d structure from multiple images of large-scale environments. In: Lecture Notes in Computer Science (1998)
20. Lei, C.: A novel camera self-calibration technique based on the kruppa equations. Chinese Journal of Computers (2003)
21. Li, J., Yang, Y.M., Fu, G.P.: Camera self-calibration method based on ga-pso algorithm. 2011 IEEE International Conference on Cloud Computing and Intelligence Systems pp. 149–152 (2011). https://doi.org/10.1109/CCIS.2011.6045050
22. Liang, B.J., Chen, Z.Z., Pears, N.: Uncalibrated two-view metrology. Proceedings of the 17th International Conference on Pattern Recognition **1**, 96–99 (2004)
23. Liang, C., Wong, K.: Robust recovery of shapes with unknown topology from the dual space. IEEE Transactions on Pattern Analysis and Machine Intelligence **29**(12), 2205 (2007)

24. Liu, Y., Yang, J.Y., Zhou, X.Y., Ma, Q.Q., Zhang, H.: Intrinsic calibration of a camera to a line-structured light using a single view of two spheres. In: Advanced Concepts for Intelligent Vision Systems. pp. 87–98. Springer International Publishing (2018)
25. Mendonca, P.R.S.: Multiview geometry : profiles and self-calibration. Ph.D. thesis, University of Cambridge (2001)
26. Mendonca, P.R.S., Wong, K.Y., Cipolla, R.: Epipolar geometry from profiles under circular motion. IEEE Transactions on Pattern Analysis and Machine Intelligence **23**, 604–616 (2001)
27. Moré, J.J.: Levenberg–marquardt algorithm: implementation and theory (1977)
28. Projectibe, C.Z.: Affine and Euclidean Calibration in Computer Vision and the Application of Three Dimensional Perception. Ph.D. thesis, Robot Vis Group. INRIA Sophia - Antipolis (1996)
29. Semple, J., Kneebone, G.: Algebraic projective geometry. Oxford University Press (1998)
30. Sinha, S.N., Pollefeys, M., McMillan, L.: Camera network calibration from dynamic silhouettes. pp. 235–243 (2004)
31. Wang, G.H., Wu, Q.M., Zhang, W.: Kruppa equation based camera calibration from homography induced by remote plane. Pattern Recognition Letter **29**, 2137–2144 (2008)
32. Wilczkowiak, M., Boyer, E., Sturm, P.F.: Camera calibration and 3d reconstruction from single images using parallelepipeds. vol. 1, pp. 142–148 (2001)
33. Wong, K.Y., Zhang, G.Q., Liang, C., Zhang, H.: 1d camera geometry and its application to the self-calibration of circular motion sequences. IEEE Transactions on Pattern Analysis and Machine Intelligence **30**(12), 2243–2248 (2009)
34. Zhang, H., Wong, K.Y.: Self-calibration of turntable sequences from silhouettes. IEEE Transactions on Pattern Analysis and Machine Intelligence **31**, 5–14 (2009)
35. Zhang, H., Zhang, G.Q., Wong, K.Y.: Camera calibration with spheres: Linear approaches. In: IEEE International Conference on Image Processing. vol. 2 (2005)
36. Zhang, Z.Y.: A flexible new technique for camera calibration. IEEE Transactions on Pattern Analysis and Machine Intelligence pp. 1330–1334 (2000)
37. Zhang, Z.Z.: Camera calibration with one-dimensional objects. In: IEEE. pp. 892–899 (2004)